

# X-ray Standing Waves in Epitaxial Thin Films

**A. KAZIMIROV**

*Cornell High Energy Synchrotron Source, Cornell University, Ithaca, NY 14853, USA*

**J. ZEGENHAGEN**

*European Synchrotron Radiation Facility, B.P. 220, 38043 Grenoble, France*

**M. J. BEDZYK**

*Department of Materials Science and Engineering and Materials Research Center, Northwestern University, Evanston, IL 60208, USA and Materials Science Division, Argonne National Laboratory, Argonne, IL 60439, USA*

**T.-L. LEE**

*European Synchrotron Radiation Facility, B.P. 220, 38043 Grenoble, France*

**E. SOZONTOV**

*Institute of Crystallography, Kaluga branch, 248640 Kaluga, Russia*

**V. KOHN**

*Russian Research Center "Kurchatov Institute," 123182 Moscow, Russia*

The XSW method, due to its element specificity and phase sensitivity, opens up new interesting application areas for studies of the structure of epitaxial thin films. The purpose of this article is to demonstrate the capabilities of the technique based on the experiments the authors have conducted at different SR sources over the past several years. We will limit the scope of this review to only the few applications that include precise lattice mismatch measurements, polarity determination, and impurity localization. We will show that the properties and the behavior of the standing wave in the epitaxial structure and attainable structural information depend on a combination of experimental parameters. The most important parameters are: the film thickness  $t_{\text{film}}$ , extinction length  $L_{\text{ex}}$ , lattice mismatch  $\Delta d/d = -\Delta\theta \cdot \text{ctg}\theta_B$ , determining the angular separation of the substrate and film diffraction peaks  $\Delta\theta$ , and the yield depth  $L_{\text{yl}}$  of the secondary radiation excited by the XSW field, usually fluorescence or photoelectrons.

Based on the above parameters we can describe thin film XSW experiments under the following four situations:

- (i) For a very thin film and/or high order substrate reflection, such that  $t_{\text{film}} \ll L_{\text{ex}}$ , the XSW field inside the film is not significantly affected by the presence of the film and it can be considered as generated in the thick substrate and described by the dynamical theory for a perfect crystal. The fluorescence yield from the film can be analyzed in terms of the standard XSW

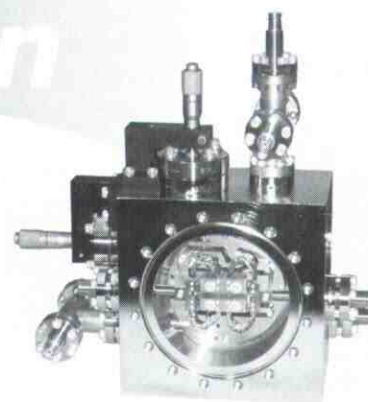
parameters, coherent position  $P$  and coherent fraction  $F$  [1]. The XSW curves will have high sensitivity to the interface structure [2, 3] and small lattice mismatch [4, 5].

- (ii) When the secondary radiation is collected from a very shallow surface layer  $L_{\text{yl}} \ll t_{\text{film}}$ , and the interface structure is known the lattice mismatch  $\Delta d/d$  between substrate and film can be measured with high precision [6, 7]. We will demonstrate this situation by our studies of the isotopic effect on the lattice constant of Ge and Si.
- (iii) For a large mismatch with  $\Delta d/d \gg \omega_{\text{sub}} \cdot \text{ctg}\theta_B$ , where  $\omega_{\text{sub}}$  is the width of the substrate rocking curve, diffraction from the film is well separated from the substrate and, for a thin film ( $t_{\text{film}} \ll L_{\text{ex}}$ ), it is essentially kinematical [8]. This situation is typical for modern ultra-thin film technology when the thickness of the film is usually constrained to be within a coherent growth mode. We will show that using 3rd generation SR sources the XSW fields generated inside few nm thick films can be reliably measured and that important parameter such as the polarity of a film with noncentrosymmetric structure can be unambiguously determined.
- (iv) Collecting the atomic fluorescence excited by the XSW field one can localize these atoms in the lattice of the film [9]. In modern semiconductor technology, impurity activation remains

# Instrumentation

**NIM, SGM, PGM  
monochromator  
beamlines &  
components.**

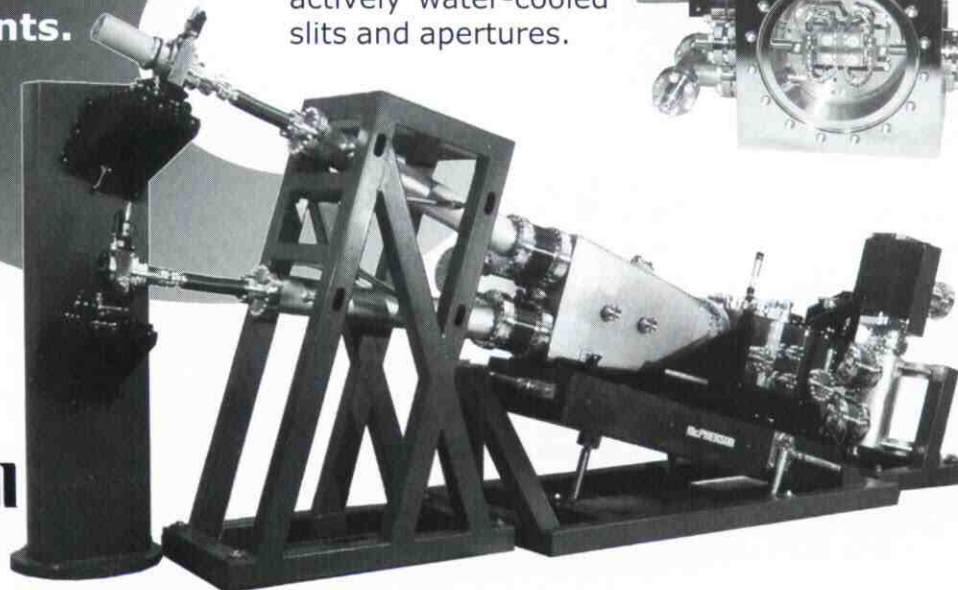
Ambient temperature,  
braid heat sink and  
actively water-cooled  
slits and apertures.



We will build your  
design or ours.

**McPHERSON**

Inquire for details.



Call 1-978-256-4512, Fax 978-250-8625, Sales@McPhersonInc.com, [www.McPhersonInc.com](http://www.McPhersonInc.com)

a most important problem. We will demonstrate that the XSW method can provide a link between structural properties and electrical behavior of dopant atoms.

To calculate the XSW field in an epitaxial structure, conventional single crystal dynamical diffraction theory is not sufficient and a more general theory of the XSW in the crystal with modified surface layer is required [10–13]. Starting in the early 1980s, experiments on epitaxial structures served as a testing ground for development of a more advanced theory. Most experimental results presented in this article were analyzed with a computer algorithm based on the theory of X-ray diffraction and XSW in multilayer crystals [13].

## Precise lattice constant measurements:

### Isotopic effect in Ge and Si

Isotopic effect on crystal volume originates from the effect of nuclear mass on the zero-point vibrations and the related anharmonicity of interatomic potentials. The effect is largest at low temperature and it is proportional to relative mass difference  $\Delta M/M$ . In the case of small  $\Delta M/M$  and a low Debye temperature, the expected changes in lattice constant  $\Delta a/a$  lie in the  $10^{-5}$  to  $10^{-6}$  range. Besides an academic interest to verify different theoretical models, this effect has important practical

implications in modern metrology.

We studied this effect in Ge [14, 15] and Si [15] by growing isotopically enriched epitaxial films ( $^{76}\text{Ge}$ ,  $\bar{M} = 75.63$ , and  $^{30}\text{Si}$ ,  $\bar{M} = 29.2$ ) on single crystal substrates of different isotopic composition (natural Ge,  $\bar{M} = 72.59$ , isotopically enriched  $^{70}\text{Ge}$ ,  $\bar{M} = 70.08$ , and natural Si,  $\bar{M} = 28.14$ ). We then used the XSW method to precisely measure the corresponding lattice constant differences.

The measurements were performed in a cryostat in a temperature range from the room temperature (RT) to 30K. Photoelectrons excited by the XSW field were collected with a channeltron at a grazing exit angle to satisfy the critical condition of keeping the yield depth  $L_{yi}$  very small. When the XSW signal is collected from the topmost layer the interference term in the XSW yield acquires an additional phase shift  $2\pi \cdot P = 2\pi \cdot N \cdot (\Delta d/d)$ . Thus, an XSW measurement determines the total shift of the surface  $N \cdot \Delta d = t \cdot (\Delta d/d)$ , where  $N$  is the number of lattice planes in the film and  $t$  is the thickness of the film. Because of the moderate crystal quality of the  $^{70}\text{Ge}$  substrate with mosaic spread of 0.3 deg, XSW measurements were performed in backscattering geometry using the (444) reflection. The experimental setup used at the HASY-LAB RÖMO station is shown in Figure 1a. The photoelectron yield from a 0.56  $\mu\text{m}$  epitaxial  $^{76}\text{Ge}$  layer on  $^{70}\text{Ge}$  is shown in Figure 1b for differ-



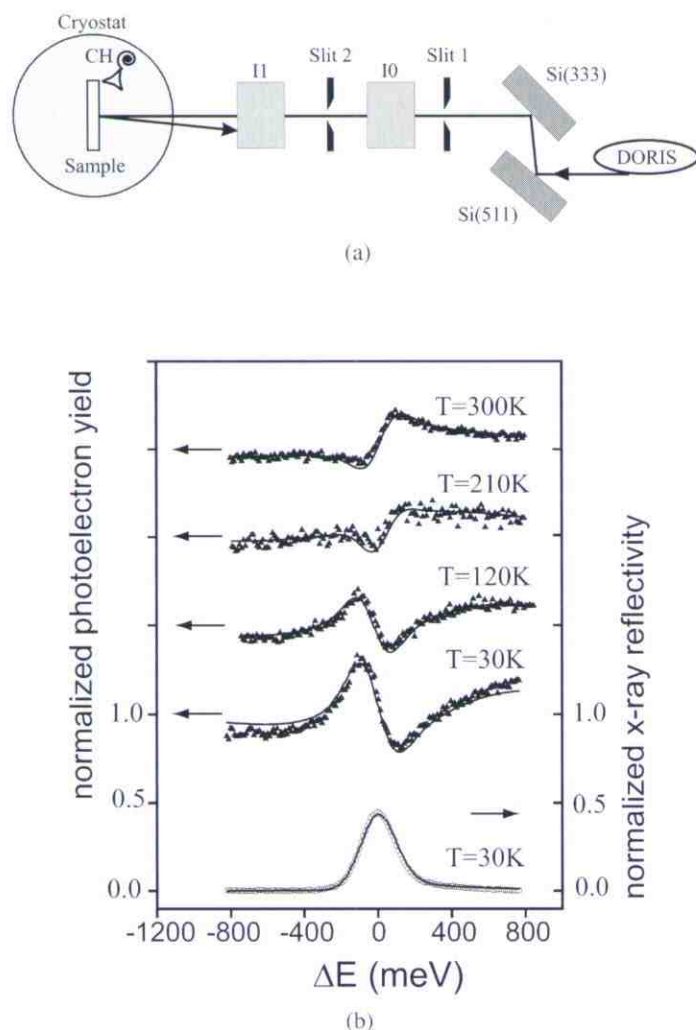


Figure 1: (a) Experimental setup at the RÖMO station at HASYLAB used for the XSW analysis of the isotopic effect on lattice constant of Ge is shown. Backscattering geometry was used to overcome mosaicity of the  $^{70}\text{Ge}$  substrate. The photoelectron yield was collected by channeltron (CH) at the grazing exit angle. (b) X-ray reflectivity and photoelectron yield for different temperatures from a  $0.56\text{ }\mu\text{m}$  epitaxial  $^{76}\text{Ge}$  layer on  $^{70}\text{Ge}$  as a function of energy  $\Delta E$  for the (444) reflection [15]. The solid lines are fits to the experimental data (symbols). The phase shift approximately by  $\pi$  is clearly observed as the sample is cooled down to 30 K corresponding to the total shift of the surface of  $\approx 0.4\text{ }\text{\AA}$ .

ent temperatures. One can clearly observe the phase of the XSW curves changing approximately by  $\pi$  as the temperature goes down from the room temperature (RT) to 30 K. This phase shift corresponds to a total shift of the surface by  $d_{444}/2 \approx 0.4\text{ }\text{\AA}$ . With knowledge of the film thickness and elastic constants, the difference in lattice constant can be deduced [14]. For Ge and Si and a mass difference of  $\Delta M = 1\text{ amu}$  we found at RT (30 K) a lattice constant difference of  $\Delta a/a = -0.36 \times 10^{-5}$  ( $-0.88 \times 10^{-5}$ ) and  $-1.8 \times 10^{-5}$  ( $-3.0 \times 10^{-5}$ ), respectively. The error in  $\Delta d/d$ , which is smaller than  $10^{-6}$  in these experiments, can be further reduced by choosing higher order reflections. New experiments to measure the influence of the isotopic mass on the lattice constant of compound semiconductors are in progress.

#### Polarity measurements: GaN thin films

Most semiconductor crystals are noncentrosymmetric and exhibit different physical and chemical properties on faces distinguished by polarity. From early on the XSW technique was established as a sensitive tool for unambiguously determining polarity. Experiments were successfully performed by different research groups on perfect single crystals such as GaP [16, 17], CdS [18], GaAs [19, 20], CdTe [21]. Recently, interest in this problem has been revived with advances in gallium nitride thin film technology. In GaN based heterostructures, polarity is one of the major factors determining confinement of a two-dimensional electron gas at the interface [22]. Polarity is not easily predicted and a direct technique is needed to determine it experimentally.

We applied the XSW method to determine polarity of thin GaN films grown by plasma induced molecular beam epitaxy (PIMBE) on sapphire [23], and by hydride vapor phase epitaxy (HVPE) on the Si-face of SiC [24]. The basic idea of the technique is illustrated by Fig. 2a where two GaN structures, with Ga- and N- faces, are shown together with the positions of the XSW antinodal planes at the low- and high-angle side of the rocking curve. Experimental Ga-K fluorescence yield curves are shown in Figure 2b. Surprisingly, we found [23] that a GaN film grown on sapphire by MBE shows N polarity (left panel in Figure 2b), which is opposite to the Ga polarity of the film grown on the same substrate by metal-organic chemical vapor deposition (MOCVD). This finding provides important insight to control electrical characteristics of GaN heterostructure field-effect transistors [22]. For the GaN film grown by HVPE on the Si-face of SiC (Figure 2b, right panel) the Ga polarity was unambiguously determined [24].

A remarkable feature of these and other thin film XSW experiments (e.g. on high-temperature superconductor (HTS) [8, 25] and the ferroelectric films, described in the next section) is that these materials, from the dynamical diffraction point of view, are highly imperfect. Even the best quality GaN films show dislocation density in the range of  $10^7$  to  $10^8\text{ cm}^{-2}$  [24]. One would not expect to apply the "standard" XSW method to such materials, but because diffraction is essentially kinematical and the rocking curve is broad, the thin film XSW technique is very forgiving. However, the experimental cost of "going thin" is that

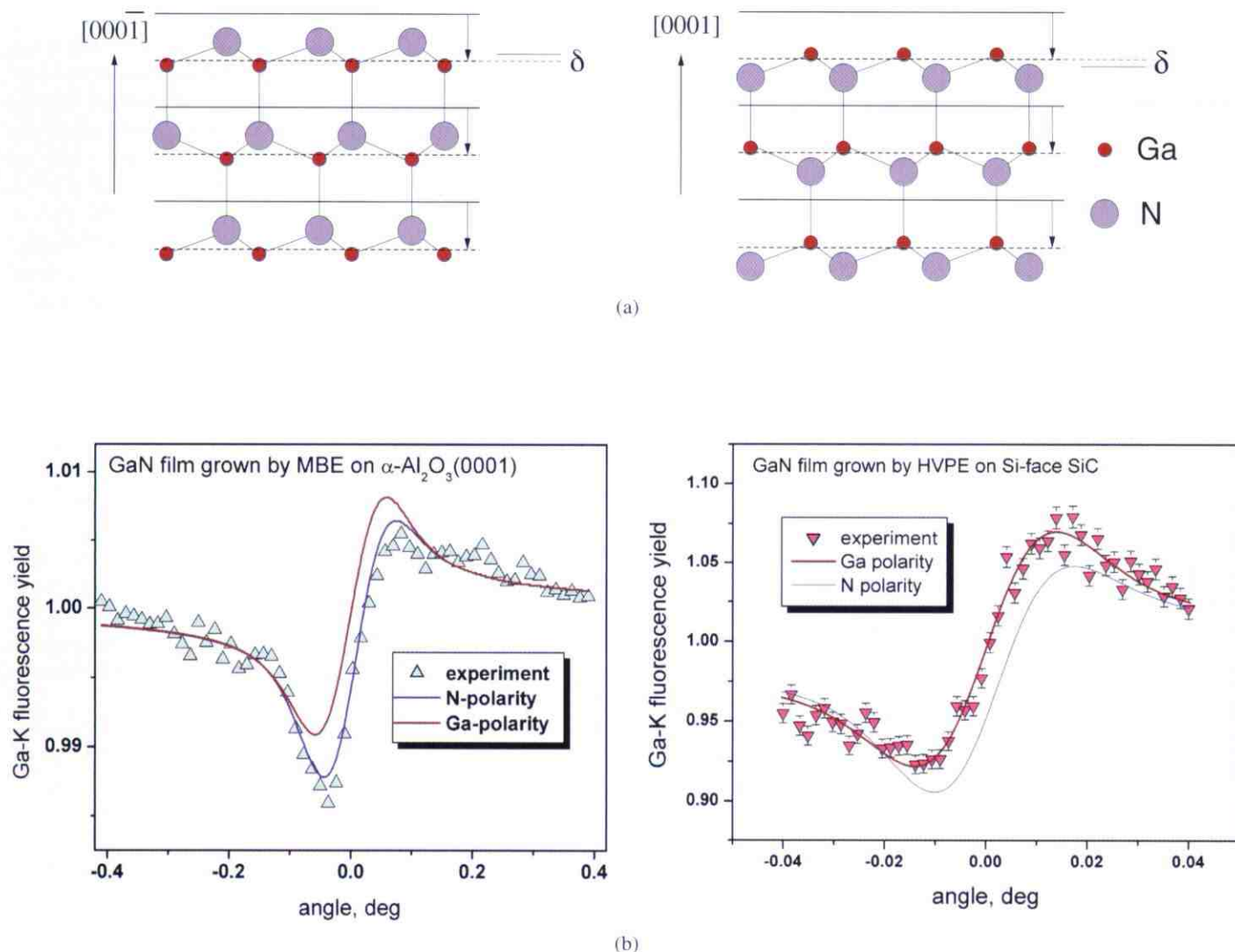


Figure 2: Determination of the polarity of thin film with noncentrosymmetric structure. (a) Crystal structure of GaN for N- (left) and Ga- (right) faces. The positions of the antinodal XSW planes at the low angle side of the rocking curve (RC) are shown as solid lines and at the high angle side of the RC as dashed lines. The downward pointing arrows indicate the inward shift of the antinode by half of  $d_{0002}$  while crossing the GaN(0002) Bragg peak. (b) Experimental XSW data collected from the GaN film grown by plasma induced molecular beam epitaxy on sapphire ([23], left panel) and by hydride vapor phase epitaxy on Si-face SiC ([24], right panel). The N-polarity was unambiguously determined in the first case and the Ga-polarity in the second one.



the XSW interference field is weak. The thinner the film, the lower the reflectivity  $R$ , and the weaker the visibility of the XSW interference fringes  $V \approx 2\sqrt{R}$ . In our experiments we demonstrated that with modern SR beams, modulations of few percent or even less in the fluorescence yield produced by a very weak XSW field can be reliably measured.

### Polarization switching in thin ferroelectric films

The direction of polarization in ferroelectric crystals can be switched by an external electric field and this provides the basis for non-volatile random access memory [26]. On the atomic level this phenomenon involves a shift of different ion lattices relative to each other. Recently, single crystal ferroelectric thin films with thickness much less than the typical domain size in bulk crystals have been grown using various synthesis methods. It was established [27] that for  $\text{PbTiO}_3$  films the formation of  $a$ -domains with polarization vector parallel to the surface can be totally suppressed below a critical thickness of 500–700 Å and single-crystal  $c$ -domain films are grown by MOCVD technique on  $\text{SrTiO}_3(001)$  substrates. The tetragonal *up* and *down*  $\text{PbTiO}_3$  unit cells are shown in Figure 3a. Whether these  $c$ -domains are polarized up or down exclusively or whether there is a co-existence of both domain types is not obvious. To answer this question we applied the thin film XSW technique to study the structure of  $\text{PbTiO}_3$  films with the thicknesses of 100 Å, 200 Å, and 400 Å [28]. Measurements were performed by using both (001) and (002) reflections and Pb-L and Ti-K (at grazing exit angle) fluorescence yield at several lateral positions. Our results unambiguously show a single *up* polarization state for 400 Å thick film, while for a 100 Å thick film we found both *up* and *down* domain regions. Our finding of a single polarization state in an as-grown ferroelectric film is quite intriguing considering that the transition temperature reported for bulk  $\text{PbTiO}_3$  (490°C) is much lower than the growth temperature (700–750°C). This may indicate a thickness effect or, more likely, a role for substrate surface structure, and surface atomic termination in particular, in determining polarization state in the growing film.

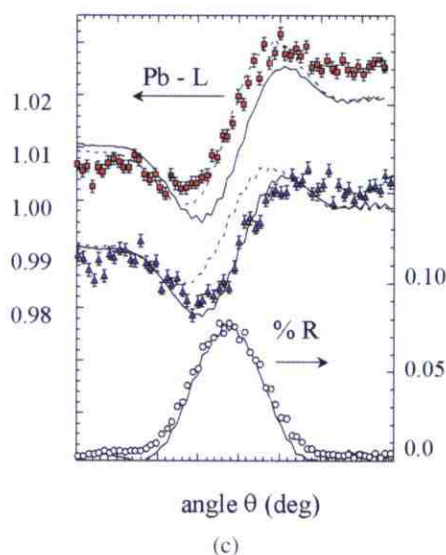
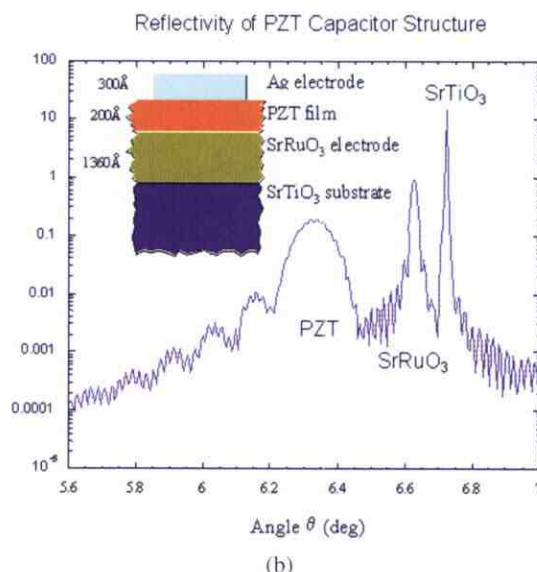
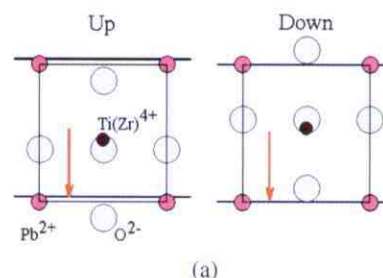


Figure 3: (a) The  $a$ -axis projection of the  $\text{PbTiO}_3$  ( $\text{Pb}(\text{Zr}_x\text{Ti}_{1-x})\text{O}_3$ , PZT) tetragonal *up* and *down* perovskite unit cells is shown. The net dipole moment is due to the displacement of the  $\text{Pb}^{2+}$  and  $\text{Ti}(\text{Zr})^{4+}$  sublattices relative to the  $\text{O}^{2-}$  sublattice. The solid lines show the position of the (001) diffraction planes. The arrows mark the inward path the XSW antinode follows while scanning through the (001) diffraction peak. (b) Experimental reflectivity of the PZT capacitor structure. The inset schematically shows the heteroepitaxial structure. (c) Experimental XSW data taken from the PZT capacitors polarized down (upper curve) and up (down curve) [29]. The best fit for the up and down domains is shown by solid lines. The measurements were performed on structures with the top Ag electrode of 250  $\mu\text{m}$  diameter. The curves were given a 0.02 vertical offset for purposes of clarity.

As a next step toward understanding polarization switching, we performed experiments on  $\text{Pb}(\text{Zr}_{0.3}\text{Ti}_{0.7})\text{O}_3$  (PZT) heterostructures that are used as a prototype of future memory cells [29]. The capacitor structure consists of a 20-nm-thick epitaxial PZT film grown on an epitaxial 136-nm-thick  $\text{SrRuO}_3$  layer (bottom electrode) deposited onto a single crystal  $\text{SrTiO}_3$  substrate (inset in Figure 3b). Polycrystalline 30-nm-thick Ag top electrodes were electron-beam evaporated through a shadow mask onto the surface of the continuous PZT film. The X-ray reflectivity (Figure 3b) shows diffraction peaks from the substrate, bottom electrode, and the PZT layer. The top electrode of a selected capacitor was connected to the output voltage of a function generator, while the bottom electrode was held at ground potential. The XSW measurements were performed on a number of capacitors after they underwent a voltage cycling that left them in one or the other polarization state. We found remarkable agreement between structural and electrical characteristics (Fig. 3c). For some structures backswitching was observed, in agreement with electrical measurements that showed a preferred orientation for these capacitors. The success of this type of measurement opens the door to more complex endeavors. For example, by combining the thin film XSW method with X-ray micro-focusing and *in-situ* biasing, one could hope to observe real-time switching with micron-scale lateral resolution and to study degradation phenomena such as imprint and fatigue [26].

## Impurity localization in semiconductor films: Zn in InP

Incorporation of bulk impurities in the lattice remains one of the most important problems in semiconductor technology. Electrically inactive dopant atoms often lead to uncontrolled diffusion, displacement of the p-n junction, changes in the built-in electric field in the active region, and deterioration of the device performance. The XSW technique can provide structural information about the position of dopant atoms in the host lattice, which is extremely important for a better understanding of the activation process on the atomic level. In our recent experiments at CHESS we studied 1  $\mu\text{m}$  thick InP epitaxial films grown by MOCVD on InP(100) substrates [30]. The films were doped during growth with Zn, the most widely used p-type dopant for InP based optoelectronics devices. The Zn concentration measured by SIMS was  $(2.4 \pm 0.2) \times 10^{18} \text{ cm}^{-3}$  and the p-type carrier concentration of  $(1.2 \pm 0.1) \times 10^{18} \text{ cm}^{-3}$  was determined by electrochemical CV profiling. The (004) XSW Zn-K fluorescence yield is shown in Figure 4 together with In-L and P-K yields from the film as well as the X-ray reflectivity curve. Strong modulation in the center is due to interference between X-ray waves scattered by the substrate and the film. This is followed by a more weak and broad XSW feature attributed to the film. The fit (solid lines) of the XSW data for the host atoms composing the film yields a static Debye-Waller factor  $f_{\text{film}} = \exp(-W_{\text{film}}) = 0.94$  with the coherent fraction and coherent position  $F_c^{\text{In,P}} = 1.0$  and  $P_c^{\text{In,P}} = 0.0$  as determined from both the In-L and P-K data. The high value of the static Debye-Waller factor indicates ex-

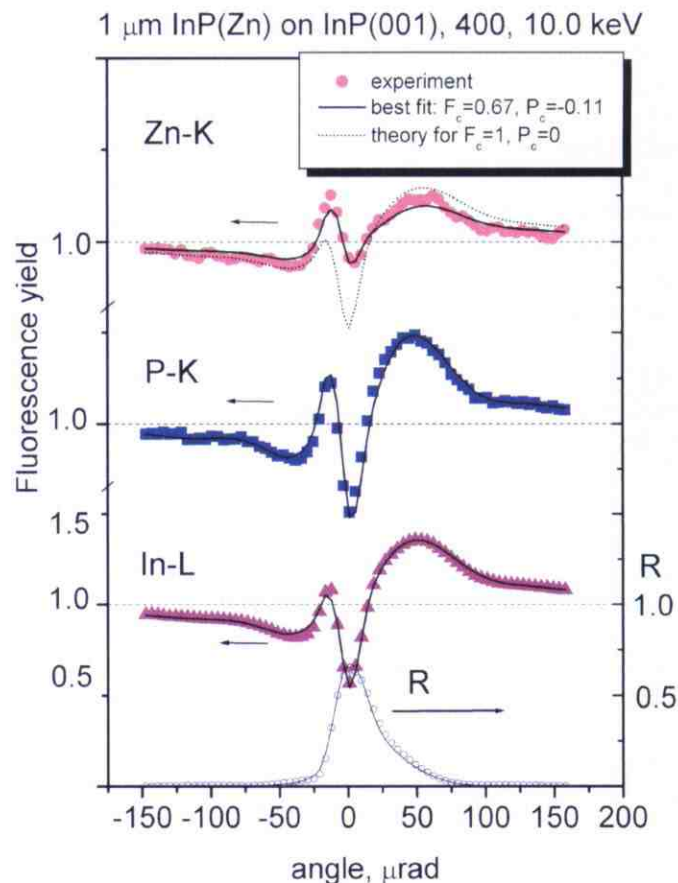


Figure 4: XSW data collected from the 1  $\mu\text{m}$  thick InP epitaxial films grown by MOCVD on InP(100) substrate and doped by Zn during the growth is presented: Zn-K fluorescence yield from the doping atoms (red circles), P-K (blue squares) and In-L (purple triangles) fluorescence from the film lattice, and the X-ray reflectivity curve R (at the bottom, right scale). The best fit is shown by solid lines. For the P-K and In-L curves the fit yields the static Debye-Waller factor  $f_{\text{film}} = 0.94$  with  $F_c^{\text{In,P}} = 1.0$  and  $P_c^{\text{In,P}} = 0.0$ . The coherent fraction for Zn atoms  $F_c^{\text{Zn}} = 0.67$  indicates that most of the electrically inactive Zn atoms (about 50%, according to CV profiling measurements) are randomly distributed in the lattice. The coherent position of  $P_c^{\text{Zn}} = -0.11$  indicates small displacement of Zn atoms from the lattice sites due to the difference in the bond lengths.

cellent crystalline quality of the film. Using the same  $f_{\text{film}}$  the fit of the Zn-K data yields  $F_c^{\text{Zn}} = 0.67$  and  $P_c^{\text{Zn}} = -0.11$ . The reduced coherent fraction  $F_c^{\text{Zn}}$ , consistent with electrical measurements, indicates that most of the electrically inactive Zn atoms are randomly distributed in the lattice, most likely taking up interstitial positions or forming clusters. The (111) XSW data (not shown) reveals that electrically active Zn occupies the In sublattice.



## Summary

Our experiments show that an XSW field can be generated by extremely thin films under conditions when diffraction becomes essentially kinematical. With modern SR sources, weak modulations in the secondary radiation yield produced by this field can be reliably measured and used for structural analysis. This opens up new avenues for studying crystalline materials that cannot be grown as perfect crystals, but can be grown only as modest quality thin films. For a more complex multilayer heterostructure one has a possibility to excite the XSW field in a particular layer by tuning the incident angle or energy. By so doing one may study the structure of the layer itself or use it as a XSW "generator" to probe the structure of layers on top of it. The theory of XSW in layered crystalline structures is well developed and demonstrates excellent agreement with experiment. When compared to traditional XSW technique that requires perfect crystal optics with a high degree of angular collimation, thin film XSW can tolerate a divergent incident beam leading to new experimental possibilities. Focusing optics producing X-ray beam with divergence of several mrad can be used for microbeam applications without deterioration of XSW pattern (see the contribution by M. Drakopoulos et al., this issue). To further increase the intensity of the incident beam multilayer optics can be used for many thin film experiments. New detection techniques based on bent analyzer crystals may prove to be more efficient when working with high intensity beams, and to provide much better energy resolution. The remarkable progress in thin film technology over the last few years makes us optimistic about new exciting experiments that will provide unique structural information about crystalline materials that will be synthesized tomorrow. ■

## Acknowledgements

The experiments presented in this article are the result of a much broader collaboration with the researchers from different laboratories and institutions and we are very grateful to all of them. The various SR measurements made use of ROMO/HASYLAB, DND/APS, X15A/NSLS, BESSRC/APS, and A2/CHESS beamlines. Support from the European (German BMBF) and the USA (DOE, NSF, NIH) funding agencies is greatly acknowledged.

## References

1. J. Zegenhagen, *Surf. Sci. Rep.* **18**, 199–271 (1993).
2. J. Zegenhagen and J. R. Patel, *Phys. Rev. B* **41**, 5315–5318 (1990).
3. T. Niwa, M. Sugiyama, T. Nakahata, O. Sakata, H. Hashizume, *Surf. Sci.* **282**, 342–356 (1993).
4. J. Zegenhagen, K. G. Huang, B. D. Hunt, and L. J. Schowalter, *Appl. Phys. Lett.* **51**, 1776–1778 (1987).
5. A. Y. Kazimirov, M. V. Kovalchuk, and V. G. Kohn, *Sov. Tech. Phys. Lett.* **14**, 587–588 (1988).
6. S. K. Andersen, J. A. Golovchenko, and G. Mair, *Phys. Rev. Lett.*, 1141–1145 (1976).
7. M. V. Kovalchuk, V. G. Kohn, and E. F. Lobanovich, *Sov. Phys.—Solid State* **27**, 2034–2038 (1985).
8. A. Kazimirov, T. Haage, L. Ortega, A. Stierle, F. Comin and J. Zegenhagen, *Solid State Comm.* **104**, 347–350 (1997).
9. A. Y. Kazimirov, M. V. Kovalchuk, A. N. Sosphenov, V. G. Kohn, J. Kub, P. Novak, and M. Nerviva, *Acta Cryst.* **B48**, 577–584 (1992).
10. A. M. Afanasev, and V. G. Kohn, *Sov. Phys.—JETP* **47**, 154–161 (1978).
11. M. V. Kovalchuk and V. G. Kohn, *Sov. Phys. Uspekhi*, **29**, 426–446 (1986).
12. A. Authier, J. Gronkowski, and C. Malgrange, *Acta Cryst.* **A45**, 432–441 (1989).
13. V. G. Kohn, *Phys. Stat. Sol. (b)* **231**, 132–148 (2002).
14. A. Kazimirov, J. Zegenhagen, and M. Cardona, *Science* **282**, 930–932 (1998).
15. E. Sozontov, L. X. Cao, A. Kazimirov, V. Kohn, M. Konuma, M. Cardona, and J. Zegenhagen, *Phys. Rev. Lett.* **86**, 5329–5332 (2001).
16. P. Trucano, *Phys. Rev. B* **13**, 2524–2531 (1976).
17. T. Takahashi, and S. Kikuta, *J. Phys. Soc. Japan* **47**, 620–624 (1979).
18. A. Annaka, T. Takahashi, and S. Kikuta, *Jap. J. Appl. Phys.* **23**, 1637–1639 (1984).
19. J. R. Patel, and J. A. Golovchenko, *Phys. Rev. Lett.* **50**, 1858–1861 (1983).
20. M. J. Bedzyk, and G. Materlik, *Phys. Rev. B* **32**, 6456–6463 (1985).
21. B. G. Zakharov, A. Yu. Kazimirov, V. G. Kohn, E. A. Sozontov, A. N. Sosphenov, *Sov. Tech. Phys. Lett.* **15**, 885–887 (1989).
22. O. Ambacher, J. Smart, J. R. Shealy, N. G. Weimann, K. Chu, M. Murphy, W. J. Schaff, L. F. Eastman, R. Dimitrov, L. Wittmer, M. Sturmann, W. Rieger, and J. Hilsenbeck, *J. Appl. Phys.* **85**, 3222–3233 (1999).
23. A. Kazimirov, G. Scherb, J. Zegenhagen, T. L. Lee, M. J. Bedzyk, M. K. Kelly, H. Angerer, O. Ambacher, *J. Appl. Phys.* **84**, 1703–1705 (1998).
24. A. Kazimirov, N. Faleev, H. Temkin, M. J. Bedzyk, V. Dmitriev, and Yu. Melnik, *J. Appl. Phys.* **89**, 6092–6097 (2001).
25. A. Kazimirov, L. X. Cao, G. Scherb, L. Cheng, M. J. Bedzyk, and J. Zegenhagen, *Solid State Comm.* **114**, 271–276 (2000).
26. O. Auciello, J. F. Scott, and R. Ramesh, *Physics Today*, **51**, 22–27 (1998).
27. C. M. Foster, Z. Li, M. Buckett, D. Miller, P. M. Baldo, L. E. Rehn, G. R. Bai, D. Guo, H. You, and K. L. Merkle, *J. Appl. Phys.* **78**, 2607–2622 (1995).
28. M. J. Bedzyk, A. Kazimirov, D. L. Marasco, T.-L. Lee, C. M. Foster, G.-R. Bai, P. F. Lyman, D. T. Keane, *Physical Review B, Rapid Comm.* **61**, R7873–R7876 (2000).
29. D. L. Marasco, A. Kazimirov, M. J. Bedzyk, T.-L. Lee, S. K. Streiffer, O. Auciello, and G.-R. Bai, *Appl. Phys. Lett.* **79**, 515–517 (2001).
30. A. A. Sirenko, A. Kazimirov, A. Ougazzaden, to be published.

Copyright of Synchrotron Radiation News is the property of Taylor & Francis Ltd and its content may not be copied or emailed to multiple sites or posted to a listserv without the copyright holder's express written permission. However, users may print, download, or email articles for individual use.